ELSEVIER

Journal of Physics and Chemistry of Solids 63 (2002) 765–772

JOURNAL OF PHYSICS AND CHEMISTRY OF SOLIDS

www.elsevier.com/locate/jpcs

Structural studies of nanocrystalline SnO_2 doped with antimony: XRD and Mössbauer spectroscopy

B. Gržeta[a,*], E. Tkalčec[b,1], C. Goebbert[b], M. Takeda[c], M. Takahashi[c], K. Nomura[d], M. Jakšić[e]

[a]*Division of Materials Chemistry, Ruđer Bošković Institute, P.O. Box 180, 10002 Zagreb, Croatia*
[b]*Institut für Neue Materialien, 66123 Saarbrücken, Germany*
[c]*Department of Chemistry, Faculty of Science, Toho University, Funabashi, Chiba 274-0072, Japan*
[d]*School of Engineering, University of Tokyo, Hongo 7-3-1, Bunkyo-ku, Tokyo 113-8656, Japan*
[e]*Division of Experimental Physics, Ruđer Bošković Institute, P.O. Box 180, 10002 Zagreb, Croatia*

Received 18 May 2001; received in revised form 21 August 2001; accepted 7 September 2001

Abstract

A series of Sb-doped SnO_2 samples, with doping levels 0, 3.1, 6.2, 11.9 and 14.0 at% Sb, has been hydrothermally prepared and characterized by X-ray powder diffraction. Diffraction lines were broadened, the line broadening being anisotropic. Both the line broadening and line anisotropy were dependent on the Sb doping level. The samples are tetragonal, space group $P4_2/mnm$ and isostructural with TiO_2(rutile). Sb doping of SnO_2 causes the increase of unit-cell parameters. The structure of pure SnO_2 and of samples containing 6.2 and 11.9 at% Sb has been refined by the Rietveld method. Crystal structure indicated that both Sb^{3+} and Sb^{5+} are substituted for Sn^{4+} in the SnO_2 structure, Sb^{3+} being dominant for the investigated doped samples. The samples were also examined by ^{119}Sn- and ^{121}Sb-Mössbauer spectroscopy. Mössbauer spectroscopy confirmed the XRD results. Also, the values of the isomer shifts and quadrupole coupling constants indicated that the configuration around the Sb^{3+} site includes the presence of the stereochemically active lone pair electrons.

Keywords: A. Oxides; B. Sol–gel growth; C. X-ray diffraction; C. Mössbauer spectroscopy; D. Crystal structure

1. Introduction

SnO_2 (cassiterite) posseses a tetragonal TiO_2 (rutile)-type structure [1], in the space group $P4_2/mnm$. It is a wide-band gap semiconductor ($E_g = 3.97$ eV) with transmittance cut-off at 333 nm [2]. When doped with F, Sb or Mo it becomes a conductor, while its optical transmittance is invariant [3,4]. Because of these properties, SnO_2 has been a widely used material for various optoelectronic applications, such as thin film transparent conductors in electroluminescent devices, solar cells, etc. [3,5].

In the case of antimony doping, it was evidenced that the resistivity decreased for lightly-doped SnO_2, while it increased for heavily-doped SnO_2 [6]. Also, it was noticed that heavily-doped SnO_2 was deeply coloured [7]. Up to now many structural studies have been devoted to antimony doped SnO_2 to elucidate the above phenomena, but still there are uncertainties as to how antimony is incorporated into the SnO_2 structure. Tsunashima et al. [8] found no trace of any other crystalline phase but cassiterite in the diffraction pattern of thin SnO_2 films containing up to 30 at% Sb, and heat-treated at 600°C. However, the diffraction lines were broad; for larger antimony content the lines were broader. The authors explained this effect by possible incorporation of amorphous antimony oxide into cassiterite. Kikuchi and Umehara [9] found that the largest amount of antimony incorporated at about 1000°C was 2.3 at% Sb. They assumed formation of a solid solution $Sb_xSn_{1-x}O_2$, with antimony in the Sb^{5+} state incorporated into a cassiterite structure. The lattice parameters were constant up to 0.5 at% Sb, while between 0.5 and 2.3 at% Sb the lattice parameters increased linearly with the antimony content.

* Corresponding author. Tel.: +385-1-4561120; fax: +385-1-4680098.
E-mail address: grzeta@rudjer.irb.hr (B. Gržeta).
[1] Present address: Faculty of Chemical Engineering and Technology, University of Zagreb, Marulićev trg 20, 10000 Zagreb, Croatia.

0022-3697/02/$ - see front matter
PII: S0022-3697(01)00226-8

Higher amount of antimony caused a separation of the system into two phases, Sb_2O_4 and SnO_2, respectively. Studying the crystallization of amorphous Sb–Sn–O thin films sprayed onto glass substrates, Kojima et al. [10] found a non-linear increase of the lattice parameters of the crystal (cassiterite) phase, which they attributed to the presence of antimony in two different oxidation states, Sb^{3+} and Sb^{5+} [11]. However, they proved the coexistence of both antimony oxidation states only by blackening of the films heat-treated at 500°C. Crnjak-Orel et al. [4] also observed the non-linear dependence of the lattice parameters of antimony-doped cassiterite on the antimony content. Terrier et al. [12] tried to determine the actual doping level of Sb in the doped SnO_2 films, and also the oxidation state of incorporated antimony, by means of X-ray photoelectron spectroscopy (XPS) and secondary ion mass spectroscopy (SIMS). They found that in doping the Sb^{3+} overcame the Sb^{5+} content, but they could not ascertain the exact content of antimony for which this occurred. The present paper reports the preparation of powder samples of SnO_2 containing antimony in amounts up to 14.0 at% Sb and their structural characterization. Locating antimony in the cassiterite structure was achieved by means of the Mössbauer spectroscopy and the Rietveld structure refinement.

2. Experimental procedure

2.1. Sample preparation

The powder samples of pure SnO_2 and ones doped with antimony in the amounts of 3.1, 6.2, 11.9 and 14.0 at% (the samples *S*0–*S*4) were prepared using a sol–gel technique followed by hydrothermal treatment. A solution of tin(IV) chloride in ethanol containing various amounts of $SbCl_3$ was added dropwise to an aqueous ammonia solution containing 10 wt.% of the surface modifying agent, β-alanine, with respect to the oxide. The suspensions were treated at 150°C for 3 h. The resulting powders were isolated by centrifuging and washed with deionized water several times and after that hydrothermally treated at 250°C and 2.5 MPa. The samples were light yellow coloured except of pure SnO_2 which was white.

2.2. Methods

The antimony concentrations in the samples were determined by means of both the atomic emission spectroscopy, using a Jobin Yvon JY24 spectrometer, and PIXE (Particle Induced X-ray Emission) spectroscopy, using a nuclear microprobe facility with a 3 MeV proton beam and a semiconductor Si(Li) X-ray detector [13]. The *K*-series of emitted X-ray radiation from thin powder samples was used for the analysis. The results of atomic emission spectroscopy and of PIXE analysis were equal within the experimental error.

Prepared powder samples were characterized by X-ray diffraction (XRD) at room temperature (RT) using a Philips MPD 1880 counter diffractometer with monochromatized Cu *K*α radiation. The following data sets were collected: (i) XRD patterns of the samples *S*0–*S*4 mixed with silicon powder (99.999%, Koch-Light Lab. Ltd., UK) as an internal standard, scanned in steps of 0.02° (2 θ) in the 2 θ range from 10 to 100° with a fixed counting time of 5 s, for the purpose of precise determination of unit-cell parameters, (ii) XRD patterns of pure samples *S*0, *S*2 and *S*3 scanned in steps of 0.06° (2 θ) in the 2 θ range from 10 to 140° with a fixed counting time of 10 s, for the purpose of the Rietveld structure refinement [14].

The ^{119}Sn- and ^{121}Sb Mössbauer spectroscopy was performed for determination of the oxidation state of tin and antimony in the samples. ^{119}Sn Mössbauer spectra were recorded at RT by a conventional transmission Mössbauer spectrometer (Topological System Co.) using a $Ca^{119m}SnO_3$ source (37 MBq) and a NaI(Tl) scintilation detector. ^{121}Sb Mössbauer spectra were measured by a Wissel Mössbauer spectometer system using a $Ca^{121m}SnO_3$ source (16 MBq) and a germanium solid-state detector; in these measurements both the source and the samples containing antimony were kept at 12 K in a cryostat incorporating a closed-cycle refrigerator [15].

2.3. Data processing

The XRD data of samples with admixed silicon powder were employed for precise determination of unit-cell parameters. The method proposed by Toraya [16] was used. Bragg angle positions, 2 θ, of seven diffraction lines of the examined sample and of three diffraction lines of silicon were determined by the individual profile fitting method (program PROFIT [17]) and taken as input data for the program UNITCELL [16]. The polynomial model of the peak shift correction function was applied. Then, the unit-cell parameters were refined by the whole-powder-pattern fitting method using the program WPPF [17]. The fitting was performed using the split-type pseudo-Voigt profile function and the polynomial background model. Anisotropic line broadening was taken into account in the fitting procedure. The starting line profile parameters for the lines *hk*0 and *h*00 were different from those for *h*0*l* and 00*l* lines and from those for *hkl* lines, respectively.

The crystal structures of the samples *S*0, *S*2 and *S*3 were refined by the Rietveld method [14]. A starting structure model for *S*0 was the structure of cassiterite, reported for the single crystal by Baur [1]: space group $P4_2/mnm$, Sn^{4+} on 2 (*a*) sites, (0, 0, 0; 1/2, 1/2, 1/2), and O^{2-} on 4 (*f*) sites, $\pm(x, x, 0; 1/2 + x, 1/2 - x, 1/2)$, with $x = 0.307$. In this structure, the six oxygen atoms about Sn form the octahedron in which four Sn–O distances are slightly different from the other two. For the Sb-doped samples, *S*2 and *S*3, a cassiterite structure model was used in which a portion of Sn^{4+} ions was substituted by antimony ions, Sb^{3+} and Sb^{5+}.

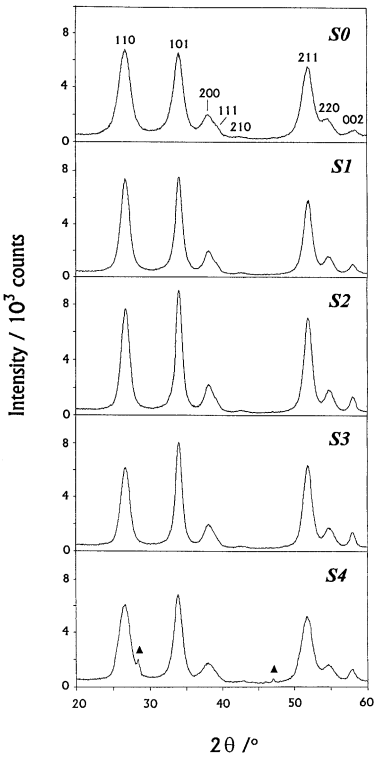

Fig. 1. Characteristic part of the XRD patterns of the samples *S*0, *S*1, *S*2, *S*3 and *S*4. Black triangles denote diffraction lines of Sb_2O_3.

Refinement was performed with the program PFLS written by Toraya and Marumo [18], using again the split-type pseudo-Voigt profile function and the polynomial background model. Six background parameters, a zero-point shift, the unit-cell parameters, three peak width parameters, three peak asymmetry parameters and two mixing parameters for the pseudo-Voigt function were included in the refinement, with structural parameters. Atomic scattering factors for Sn^{4+} ion (the same value for Sb^{5+} ion) and Sb^{3+} ion were taken from the International Tables for X-ray Crystallography [19], and for O^{2-} from Tokonami [20]. Dispersion corrections were also applied. Isotropic thermal vibration modes were assumed for all atoms.

The ^{119}Sn Mössbauer spectra were computer-fitted with one quadrupole doublet of Sn(IV) using the MossWinn program [21], and the isomer shifts (δ) were determined relative to SnO_2 at RT. The ^{121}Sb Mössbauer spectra were analyzed using a transmission integral method [22] assuming 12 quadrupole-split lines, while the isomer shifts were determined relative to InSb at 12 K.

3. Results and discussion

3.1. XRD characterization of samples

XRD patterns indicated that all the prepared samples, *S*0–*S*4, had the TiO_2(rutile)-type structure [23]. Only sample *S*4 contained impurity, as seen in Fig. 1, namely ~5 wt.% Sb_2O_3 (i.e. ~2.7 mol% Sb_2O_3). Refined unit-cell parameters of the samples are listed in Table 1 along with the literature data for cassiterite [1,25]. Both *a* and *c* parameters for the samples *S*1, *S*2 and *S*3 increased with Sb-doping level, while for *S*4 decreased to the values which could be situated between those for *S*0 and *S*1. If we consider the ionic radii for the 6-coordinated Sn^{4+} (0.83 Å), Sb^{3+} (0.90 Å) and Sb^{5+} (0.74 Å) [26], such behaviour of the cell parameters may indicate a possibility that both Sb^{3+} and Sb^{5+} ions were substituted for Sn^{4+} in the samples *S*1–*S*4, with variable Sb^{3+}/Sb^{5+} content ratio. The ratio *c*/*a* was constant for all samples having the value characteristic for the cassiterite structure, 0.672.

Diffraction lines were broadened (Fig. 1 and Table 2), indicating the nanosized crystallites in the samples. The lines of sample *S*0 showed the greatest broadening. Incorporation of antimony up to 11.9 at% Sb (sample *S*3) lessened the broadening, while for the sample *S*4 the broadening was bigger again. Also, the line broadening

Table 1
Composition of Sb-doped SnO_2 samples and refined values of their unit-cell parameters; space group $P4_2/mnm$ (136). R_p and R_{wp} are the discrepancy factors which characterize a quality of fitting result [24]

Sample notation	Antimony doping level (at% Sb)	R_p	R_{wp}	*a* (Å)	*c* (Å)	*c*/*a*	*V*(Å^3)
SnO_2[a]				4.737(1)	3.185(1)	0.672	71.47
SnO_2[b]				4.7367(1)	3.1855(1)	0.672	71.471
*S*0	0	0.044	0.063	4.7331(4)	3.1815(4)	0.672	71.273(3)
*S*1	3.1(4)	0.049	0.072	4.7399(5)	3.1854(4)	0.672	71.565(2)
*S*2	6.2(6)	0.042	0.065	4.7402(5)	3.1856(4)	0.672	71.579(2)
*S*3	11.9(5)	0.037	0.053	4.7406(4)	3.1865(4)	0.672	71.611(2)
*S*4	14.0(7)[c]	0.049	0.073	4.7379(4)	3.1830(4)	0.672	71.451(2)

[a] Data quoted from Baur [1].
[b] Data quoted from Haines and Léger [25].
[c] The total amount of antimony found in the sample *S*4 was 19.4(7) at%. A part of it (5.4 at% Sb) crystallized as Sb_2O_3 (namely 5 wt.% Sb_2O_3), as found by XRD.

Table 2
Full-widths at half-maximum (*FWHM*) for the selected diffraction lines of the samples and crystallite sizes in the direction normal to the planes (110) and (101), respectively

Sample	FWHM (° 2 θ)				$D_{\perp\,(110)}$	$D_{\top(101)}$
	110	211	002	101	(nm)	(nm)
*S*0	1.892(8)	1.829(8)	1.724(8)	1.647(8)	4(1)	5(1)
*S*1	1.449(7)	1.405(7)	1.306(7)	1.107(7)	6(2)	8(2)
*S*2	1.409(6)	1.395(6)	1.018(6)	0.936(6)	6(2)	9(3)
*S*3	1.356(6)	1.297(6)	0.918(6)	0.813(6)	6(2)	11(3)
*S*4	1.838(8)	1.813(8)	1.373(8)	1.260(8)	4(1)	7(2)

was anisotropic: the lines *hk*0 and *h*00 were systematically broader, while the lines *h*0*l* and 00*l* were systematically narrower than the *hkl* lines. The line 101 was the narrowest one for all the samples. A possible explanation of such a character of the line broadening is proposed in Section 3.2. The crystallite sizes for the samples were determined by a well-known Scherrer formula [27] from diffraction lines 110 (the broadest one) and 101 (the narrowest one), and the values are listed in Table 2.

3.2. Rietveld structure refinement

The observed and calculated powder patterns for the samples *S*0, *S*2 and *S*3 are presented in Fig. 2. Refined structural parameters are given in Table 3. The refinement for pure SnO_2, sample *S*0, confirmed the TiO_2(rutile)-type structure. In the case of the Sb-doped samples, *S*2 and *S*3, refinement was started using a cassiterite structure model in which antimony in its whole content was incorporated as

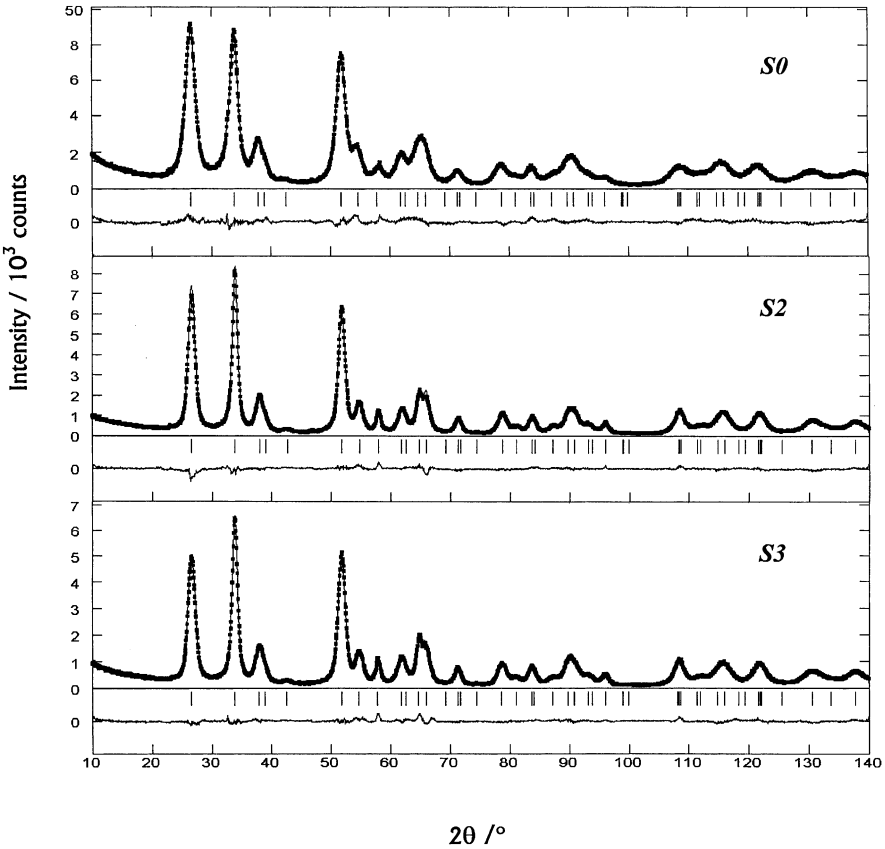

Fig. 2. Results of the Rietveld refinement for the samples *S*0, *S*2 and *S*3. The observed profile intensity is represented by black squares and the calculated intensity by the solid line. Differences between the two intensities are plotted at the bottom of the diagrams on the same scale. Vertical bars are the reflection position markers. R_p and R_{wp} values are given in Table 3.

Table 3
Structural parameters and their standard deviations for the samples *S*0, *S*2 and *S*3. R_p and R_{wp} are the discrepancy factors which characterize a quality of fitting result [24]

Sample	R_p	R_{wp}	Ion	Wyckoff position	Occupancy parameter	x	B_{iso} (Å^3)
SnO_2[a]			Sn^{4+}	2(*a*)	1		
			O^{2-}	4(*f*)	1	0.307(1)	
						0.3070(4)[b]	
*S*0	0.057	0.077	Sn^{4+}	2(*a*)	1		0.53(3)
			O^{2-}	4(*f*)	1	0.3066(7)	1.43(7)
*S*2	0.054	0.072	Sn^{4+} }		0.96		0.19(2)
			Sb^{5+} }	2(*a*)			
			Sb^{3+}	2(*a*)	0.04(2)		0.19(2)
			O^{2-}	4(*f*)	0.94(3)	0.3073(6)	1.09(20)
*S*3	0.052	0.069	Sn^{4+}}	2(*a*)	0.91		0.59(3)
			Sb^{5+}}				
			Sb^{3+}	2(*a*)	0.09(2)		0.59(3)
			O^{2-}	4(*f*)	0.91(4)	0.3074(6)	1.49(27)

[a] Data quoted from Baur [1].
[b] Data quoted from Haines and Léger [25].

Sb^{3+}, substituting for Sn^{4+}. During refinement a possibility of Sb^{5+} incorporation was taken into consideration as well. The occupancy parameter of Sb^{3+} was varied, but the sum of occupancy parameters for (Sn^{4+}, Sb^{5+}) and Sb^{3+} was kept constant, i.e. equal to unity. Refinements converged to $R_{wp} = 0.119$ and 0.136, respectively. With the introduction of oxygen occupancy parameter into refinements, R_{wp} decreased to 0.072 for *S*2, and to 0.069 for *S*3. These refinement results proved that samples *S*2 and *S*3 have the oxygen-deficient rutile-type structure in which both Sb^{3+} and Sb^{5+} ions substituted for Sn^{4+}, Sb^{3+} being dominant. In *S*2 (containing 6.2 at% Sb) antimony is incorporated as 4 at% Sb^{3+} and 2.2 at% Sb^{5+}, while *S*3 (containing 11.9 at% Sb) incorporated 9 at% Sb^{3+} and 2.9 at% Sb^{5+}. Found oxygen deficiency in *S*2 and *S*3 is the consequence of a charge imbalance due to Sb^{3+} substituting Sn^{4+}. Table 4 lists selected metal–oxygen distances derived from the final atomic parameters in Table 3. In the SnO_6-octahedra of cassiterite six Sn–O distances are equal within the limits of error. In the Sb-doped samples four Sn/Sb–O distances remain unchanged, while two others are longer by 0.44%. However, it is to be noted that this is an overall structural picture. In the vicinity of an oxygen vacancy there should be a lone pair of electrons instead of a metal–O bond.

Table 4
Selected interatomic distances (Å) and their standard deviations for the samples *S*0, *S*2 and *S*3

Sample	Interatomic distances (Å)	
	Four distances $(Sn–O)_1$	Two distances $(Sn–O)_2$
SnO_2[a]	2.052(5)	2.056(7)
*S*0	2.051(2)	2.052(2)
	Four distances $(Sn/Sb–O)_1$	Two distances $(Sn/Sb–O)_2$
*S*2	2.051(2)	2.060(3)
*S*3	2.051(2)	2.061(3)

[a] Data quoted from Baur [1].

If we look at Fig.1 and the data in Table 2 in the light of the above results, the line anisotropy can be explained as follows. In the series from sample *S*0 to sample *S*3 the incorporated Sb^{3+} content increases, and the oxygen deficiency increases as well. So, it seems that the oxygen deficiency enlarges the line anisotropy, with the line 101 being the narrowest one, and also reduces the line broadening. This conforms with the work reported by Geurts et al. [28]. They found that a little deformation in the tin matrix of SnO_2 caused by the oxygen deficiency can induce the appearance of a layered structure, which is manifested by anisotropy in the XRD line widths, with the 101 line being the narrowest one. Also, the layered structure leads to the increase in crystallite sizes, and decrease in line broadening. In the case of *S*4 appeared an impurity phase Sb_2O_3. For that reason, it is obvious that the incorporated Sb^{3+} content in *S*4 (and oxygen deficiency) does not follow the pattern noticed for the above series. Indeed, the line anisotropy for *S*4 is smaller than for *S*3, and lines of *S*4 are much broader.

3.3. Mössbauer spectroscopy

The ^{119}Sn Mössbauer spectra of the samples *S*1–*S*4 recorded at RT are shown in Fig. 3, and Mössbauer parameters: isomer shift (δ) and quadrupole coupling constant (e^2qQ) are listed in Table 5. The results indicate that there is no tin valence state else than Sn(IV) present in the samples. The non-zero quadrupole splitting indicates the existence of oxygen vacancies around Sn^{4+} ions. The value of isomer shift which is for all the samples slightly different from that

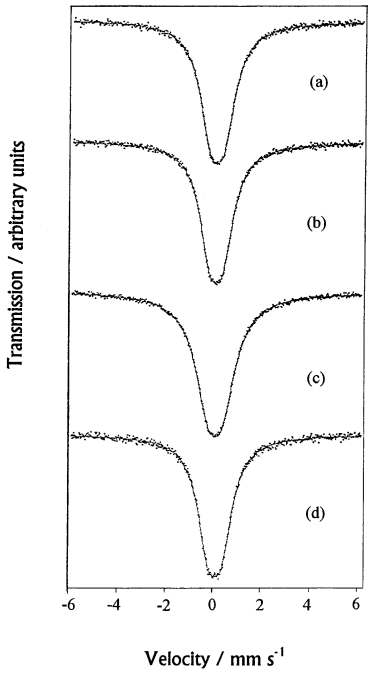

Fig. 3. ^{119}Sn Mössbauer spectra of: (a) sample *S*1, (b) sample *S*2, (c) sample *S*3 and (d) sample *S*4, recorded at room temperature.

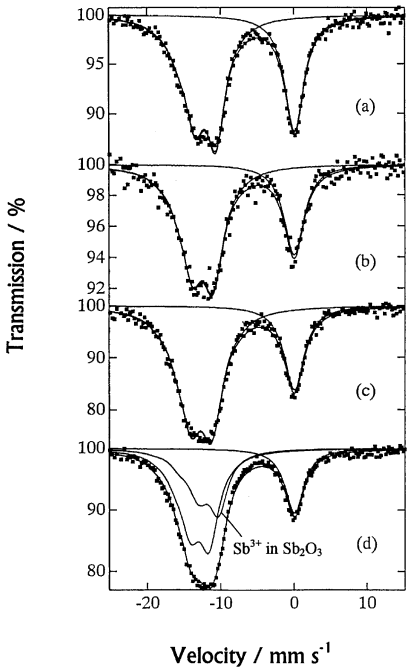

Fig. 4. ^{121}Sb Mössbauer spectra of (a) sample *S*1, (b) sample *S*2, (c) sample *S*3 and (d) sample *S*4, recorded at 12 K.

of pure SnO_2 ($\delta = 0$ mm s^{-1}) suggests a small variation in the Sn–O bond length compared to the one in pure SnO_2.

The ^{121}Sb Mössbauer spectra of the samples *S*1–*S*4 measured at 12 K are presented in Fig. 4. The broad asymmetric maxima at around -12 mm s^{-1} are due to Sb^{3+} and the symmetric maxima at 0 mm s^{-1} to Sb^{5+}. The least square curve fitting was performed by assuming one Sb^{5+} site and one Sb^{3+} site in the samples *S*1–*S*3. In *S*4, one Sb^{5+} site and two Sb^{3+} sites were assumed, namely that of Sb^{3+} incorporated into SnO_2 structure and that of Sb^{3+} in Sb_2O_3 since 5 wt.% of Sb_2O_3 was detected in *S*4 by XRD. The Mössbauer parameters for Sb^{3+} site in Sb_2O_3 were fixed in calculations. Isomer shift (δ), quadrupole coupling constant (e^2qQ), asymmetric parameter (η), experimental linewidth (Γ_{exp}) and relative peak area (A) for the examined samples are summarized in Table 6.

Both δ and e^2qQ values for Sb^{3+} in *S*1 are similar to those for Sb^{3+} in Sb_2O_3. This suggests that the environment around Sb^{3+} in *S*1 is similar to that in Sb_2O_3, which has three short (1.977–2.023 Å) and two longer (2.518, 2.619 Å) Sb–O bonds and a lone pair of antimony electrons [29]. The values of δ and e^2qQ for Sb^{3+} sites reflect sensitively the stereochemical activity of the lone pair of electrons and indicate the type of oxygen coordination [30]. It is noted that both δ and e^2qQ for Sb^{3+} decrease as the antimony content increases from *S*1 to *S*4 (Table 6), indicating that the stereochemical activity around Sb^{3+} is largest for *S*1 and decreases with the increase in antimony content. This suggests that Sn^{3+} ions are forced to substitute the octahedrally coordinated Sb^{4+}. The e^2qQ values for Sb^{5+} in *S*1–*S*4 are experimentally zero. This suggests that Sb^{5+} ion is substituting for Sn^{4+} in the centre of the octahedral hole where the electric field gradient eq vanished. This is quite natural since the ionic radius for the 6-coordinated Sb^{5+} (0.74 Å) is slightly smaller than that of Sn^{4+} (0.83 Å) [26]. The δ values for the Sb^{5+} site in *S*1–*S*4 well agree with those for double oxides having the rutile and trirutile structure: $M^{III}SbO_4$ (M = Al, δ = 8.70 mm s^{-1}) and $M^{II}Sb_2O_6$ (M = Mg, Zn, Cu; δ = 8.58–8.70 mm s^{-1}) [31].

The atomic content ratio of each species is almost equal to the relative peak area, *A*, of each species listed in Table 6. Atomic contents of Sb^{3+} and Sb^{5+} in the samples *S*1–*S*4 calculated on the basis of relative areas are listed in Table 7 along with the values obtained from XRD examination and the Rietveld refinement. The atomic contents obtained from Mössbauer data well agree with those from XRD. Also, the

Table 5
^{119}Sn Mössbauer parameters for the samples *S*1, *S*2, *S*3 and *S*4

Sample	Site	δ (mm s^{-1})	e^2qQ (mm s^{-1})
*S*1	Sn^{4+}	0.09	0.58
*S*2	Sn^{4+}	0.09	0.56
*S*3	Sn^{4+}	0.10	0.63
*S*4	Sn^{4+}	0.10	0.53

Table 6
^{121}Sb Mössbauer parameters for the samples *S*1, *S*2, *S*3 and *S*4

Sample	Site	δ (mm s^{-1})[a]	e^2qQ (mm s^{-1})	η	Γ_{exp} (mm s^{-1})	A (%)[b]
*S*1	Sb^{3+}	−3.64	17.7	0.62	3.15	66
	Sb^{5+}	8.69	0.0	0[c]	3.15	34
*S*2	Sb^{3+}	−4.01	16.7	0.53	3.23	70
	Sb^{5+}	8.63	0.0	0[c]	3.23	30
*S*3	Sb^{3+}	−4.21	16.5	0.76	3.00	74
	Sb^{5+}	8.67	0.0	0[c]	3.00	26
*S*4	Sb^{3+}	−4.47	15.8	0.58	2.92	49
	Sb^{5+}	8.69	0.0	0[c]	2.92	19
Sb_2O_3	Sb^{3+}	−3.32[c]	18.3[c]	0.36[c]	2.92	32

[a] Relative to InSb.
[b] Relative area.
[c] Fixed.

Table 7
Sb^{3+} and Sb^{5+} content in the samples *S*1, *S*2, *S*3 and *S*4 as obtained by the Rietveld refinement (RR) and Mössbauer spectroscopy (MS)

Sample	Total Sb content (at%)	Incorporated Sb^{3+} content (at%)		Incorporated Sb^{5+} content (at%)		Average Sb^{3+} content/Sb^{5+} content	Impurity Sb_2O_3(mol%)	
		RR	MS	RR	MS	RR, MS	XRD	MS
*S*1	3.1	–	2.0	–	1.1	1.8		
*S*2	6.2	4.0	4.3	2.2	1.9	2.0		
*S*3	11.9	9.0	8.8	2.9	3.1	3.0		
*S*4	19.4	–	9.5	–	3.7	2.6	2.7	3.1

value of 6.2 at% Sb^{3+} forming Sb_2O_3 (i.e. 3.1 mol% Sb_2O_3), obtained from Mössbauer relative peak area of 32% for sample *S*4 containing in total 19.4 at% Sb, agrees well with that of 5 wt.% Sb_2O_3 (i.e. 2.7 mol% Sb_2O_3) from XRD within the experimental error. It is seen that the Sb^{3+}/Sb^{5+} content ratio increases with the increase in antimony incorporated level up to sample *S*3, while for sample *S*4 it is smaller than for *S*3. For all the samples the value of ratio is greater than unity, i.e. the Sb^{3+} content is larger than Sb^{5+} content. The fact that Sb^{3+} favourably substitutes Sn^{4+} implies that the charge imbalance due to this process should be compensated by the formation of oxygen vacancies. Indeed, the oxygen occupancy parameters as obtained by the Rietveld refinement decreased with the increase in the antimony content doped (Table 3).

Furthermore, cell volume increases with the increase in Sb^{3+} content (in our case up to sample *S*3 as seen in Table 1). Replacement of Sn^{4+} by Sb^{3+} thereby induces deformation in the lattice, so substitution can occur only at the small Sb^{3+} contents. At a certain limit the host lattice excludes Sb^{3+} introduced, and Sb_2O_3 is formed as the second phase. This occurs between 10 and 15 at% Sb. When it occurs, the Sb^{3+}/Sb^{5+} content ratio in the doped sample decreases and the cell volume decreases consequently (as found for sample *S*4).

4. Conclusions

Preparation, XRD and Mössbauer spectroscopy examinations of the sample SnO_2 and the ones doped with Sb in content up to 14.0 at% Sb have been reported. The prepared samples were nanocrystalline. All the samples were tetragonal with TiO_2(rutile)-type structure. Unit-cell parameters increased with Sb content up to the doping level of ~12 at% Sb, after which they decreased. The level of Sb doping influenced the broadening of diffraction lines, and the anisotropy of the line widths. In the Sb-doped samples both Sb^{3+} and Sb^{5+} ions are substituted on the Sn^{4+} sites in the SnO_2 lattice, Sb^{3+} being dominant. Above doping level of about 12 at% Sb a second phase appeared in the system, namely Sb_2O_3.

References

[1] W.H. Baur, Acta Cryst. A 9 (1956) 515.
[2] B. Orel, U. Lavrenčič-Stangar, Z. Crnjak-Orel, P. Bukovac, M. Kosec, J. Non-Cryst. Sol. 167 (1994) 272.
[3] K.L. Chopra, S. Major, D.K. Pandya, Thin Solid Films 102 (1983) 1.
[4] Z. Crnjak-Orel, B. Orel, M. Hodeščck, V. Kaučič, J. Mater. Sci. 27 (1992) 313.

[5] B.O. Seraphin (Ed.), Solar Energy Conversion, Springer Verlag, Berlin, 1979.
[6] A. Rohatgi, T.R. Viverito, L.H. Slack, J. Am. Ceram. Soc. 57 (1974) 278.
[7] D. Elliot, D.L. Zellmer, H.A. Laitinen, J. Electrochem. Soc. 117 (1970) 1343.
[8] A. Tsunashima, H. Yoshimizu, K. Kodaira, S. Shimada, T. Matsushita, J. Mat. Sci. 21 (1986) 2731.
[9] T. Kikuchi, M. Umehara, J. Mater. Sci. Lett. 4 (1985) 1051.
[10] M. Kojima, H. Kato, M. Gatto, Philosoph. Mag. B 68 (1993) 215.
[11] M. Kojima, H. Kato, M. Gatto, J. Non-Cryst. Sol. 218 (1997) 230.
[12] C. Terrier, J.P. Chatelon, J.A. Roger, R. Berjoan, C. Dubois, J. Sol–Gel Science and Technology 10 (1997) 75.
[13] M. Jakšić, I. Bogdanović, D. Dujmic, S. Fazinić, T. Tadić, Strojarstvo 38 (1996) 279.
[14] H.M. Rietveld, J. Appl. Cryst. 2 (1969) 65.
[15] M. Takeda, Radioisotopes 24 (1985) 628.
[16] H. Toraya, J. Appl. Cryst. 26 (1993) 583.
[17] H. Toraya, J. Appl. Cryst. 19 (1986) 440.
[18] H. Toraya, F. Marumo, Rep. Res. Lab. Eng. Mater. Tokyo Inst. Technol. 5 (1980) 55.
[19] J.A. Ibers, W.C. Hamilton, International Tables for X-ray Crystallography, Vol. IV, Kynoch Press, Birmingham, 1974.
[20] M. Tokonami, Acta Cryst. 19 (1965) 486.
[21] Z. Klencsar, E. Kuzman, A. Vertes, J. Radioanal. Chem. Lett. 210 (1996) 105.
[22] G.K. Shenoy, J.M. Friedt, H. Maletta, S.L. Ruby, in: I.J. Gruverman, C.W. Seidel, D.K. Dieterly (Eds.), Mössbauer Effect Methodology, Vol. 9, Plenum Press, New York, 1974, p. 277.
[23] C. Legrand, J. Delville, C. R. Acad. Sci. Paris 236 (1953) 944.
[24] R.A. Young, E. Prince, R.A. Sparks, J. Appl. Cryst. 5 (1982) 357.
[25] J. Haines, J.M. Léger, Phys Rev. B 55 (1997) 11144.
[26] R.D. Shannon, Acta Cryst. A 32 (1976) 751.
[27] P. Scherrer, Gottin Nachricht 2 (1918) 98.
[28] J. Geurts, S. Rau, W. Richter, F.J. Schmitte, Thin Solid Films 121 (1984) 217.
[29] C. Svensson, Acta Cryst. B 30 (1974) 458.
[30] M. Takeda, M. Takahashi, R. Ohyama, I. Nakai, Hyperfine Interactions 28 (1986) 741.
[31] Y. Kajitani, M. Takahashi, M. Takeda, unpublished results.